



Cite this: *RSC Adv.*, 2024, **14**, 20230

## Synthesis of surfactant-assisted nickel ferrite nanoparticles (NFNPs@surfactant) to amplify their application as an advanced electrode material for high-performance supercapacitors

Muhammad Waheed Mushtaq,<sup>\*a</sup> Muhammad Shahbaz, <sup>b</sup> Rabia Naeem,<sup>b</sup> Shahid Bashir, <sup>c</sup> Shahzad Sharif, <sup>\*b</sup> Kainat Ali<sup>a</sup> and Naveed Aslam Dogar<sup>a</sup>

Nickel ferrite nanoparticles (NFNPs) were synthesized in an alkaline medium (pH ~ 11) using a wet chemical co-precipitation technique. To probe the effect of surfactants on the surface morphology, particle size and size distribution of nanoparticles; two surfactants, namely, cetyl trimethyl ammonium bromide (CTAB) and sodium dodecyl sulphate (SDS), were applied. The native and surfactant-assisted nickel ferrite NPs were characterized using Fourier transform infrared (FTIR) spectroscopy, X-ray diffraction (XRD), scanning electron microscopy (SEM), atomic force microscopy (AFM), dynamic light scattering (DLS) and transmission electron microscopy (TEM). The addition of surfactants (CTAB/SDS) effectively controlled the secondary growth of nickel ferrite particles and reduced their size, as examined by XRD, AFM, DLS, SEM and TEM. Characterization technique results affirmed that CTAB is a more optimistic surfactant to control the clustering, dispersion and particle size (~22 nm) of NFNPs. To identify the impact of ferrite particle size on charge storage devices, their electrochemical properties were studied by using cyclic voltammetry (CV), galvanic charge–discharge (GCD) and electrochemical impedance spectroscopy (EIS) in 1 M KOH electrolyte through three-electrode assembly.  $\text{NiFe}_2\text{O}_4@\text{CTAB}$  showed a specific capacity of 267.1 C g<sup>-1</sup>, specific capacitance of 593.6 F g<sup>-1</sup> and energy density of 16.69 W h kg<sup>-1</sup>, which was far better than the performances of other synthesized native NFNPs and  $\text{NiFe}_2\text{O}_4@\text{SDS}$  having larger surface areas.

Received 20th March 2024  
 Accepted 31st May 2024

DOI: 10.1039/d4ra02135e  
[rsc.li/rsc-advances](http://rsc.li/rsc-advances)

### 1. Introduction

Over the past decades, there has been a growing focus on the preparation and characterization of nanomaterials exhibiting distinct physical and chemical properties. The main reason for heightened interest in nanomaterials is primarily attributed to particle size, surface area and topography in the field of nanotechnology.<sup>1</sup> From the class of nanomaterials,  $\text{NiFe}_2\text{O}_4$  nanoparticles have attracted great interest for their peculiar applications in different fields. They have a vast area of utilization in the fields of ferrofluids, magnetic materials, catalysts, electronic and microwave devices, information storage and energy storage.<sup>2,3</sup>  $\text{NiFe}_2\text{O}_4$  nanoparticles play a vital role as catalysts in a number of significant reactions including oxidative dehydrogenation of hydrocarbons, alcohol decomposition, selective oxidation of carbon monoxide and hydrogen peroxide

decomposition.<sup>4</sup> In biological systems,  $\text{NiFe}_2\text{O}_4$  nanoparticles have been used for drug delivery where the conventional methodology fails to do the required task. Moreover, the use of NPs in magnetic resonance imaging (MRI), magnetic hyperthermia, and bio as well as chemosensors<sup>5</sup> is reported.

Spinel phase nanoparticles have potential applications in the field of energy storage devices. The use of  $\text{NiFe}_2\text{O}_4$  nanoparticles as the electrode material in lithium-ion batteries can be proved effective for superior electrical conductivity, specific capacity, enhanced electrochemical reactivity and more importantly the lower cost for energy production.  $\text{NiFe}_2\text{O}_4$  nanoparticles possess distinct properties such as high adsorption capacity, marvelous stability, safety, good magnetic properties and electronic tunability that make them a good candidate to remove environmental pollutants by the dint of their property of adsorption. Spinel nanoparticles are also used as sensors for the detection of trace pollutants even at lower concentrations with high sensitivity and excellent selectivity.<sup>6</sup> As  $\text{NiFe}_2\text{O}_4$  nanoparticles are environmentally friendly and abundant in nature, various researchers have studied their electrochemical performance.

<sup>a</sup>Department of Chemistry, Govt. Graduate College of Science, Wahdat Road, Lahore, Pakistan. E-mail: [waheedjaami@gmail.com](mailto:waheedjaami@gmail.com)

<sup>b</sup>Materials Chemistry Laboratory, Department of Chemistry, GC University Lahore, Pakistan. E-mail: [mssharif@gcu.edu.pk](mailto:mssharif@gcu.edu.pk)

<sup>c</sup>Department of Chemistry, University of Malaya, Kuala Lumpur, Malaysia



Previously reported  $\text{NiFe}_2\text{O}_4$  nanoparticles showed a specific capacitance of  $120 \text{ F g}^{-1}$ .<sup>7</sup> Kumar *et al.* synthesized mesoporous  $\text{NiFe}_2\text{O}_4$  nanoparticles *via* the hydrothermal method and studied the effect of the surface area of the nanoparticles on electrochemical response in a three-electrode assembly.<sup>8</sup> Saom *et al.* observed a specific capacitance of  $207 \text{ F g}^{-1}$  in  $1 \text{ M Na}_2\text{SO}_4$  electrolyte.<sup>9</sup> Geo *et al.* also reported that the larger surface area improved the performance of the nanoparticles showing a specific capacitance of  $204.9 \text{ F g}^{-1}$  at the current density of  $1 \text{ A g}^{-1}$ .<sup>10</sup> Furthermore, Arun *et al.* inferred that the specific capacitance of  $277 \text{ F g}^{-1}$  retained up to 5000 cycles by decreasing the particle size of the  $\text{NiFe}_2\text{O}_4$  nanoparticles.<sup>11</sup> It is evident from the study that morphology is one of the primary factors that can improve the electrochemical properties of the materials.<sup>12,13</sup> Thus, the researchers have been trying to synthesize electrode materials with large surface areas to enhance the electrochemical performance of energy storage devices. Hu *et al.* reported organic materials showing elemental stability as well as functional tenability for use as cathodes for energy storage devices, exhibiting significant electrochemical performance.<sup>14</sup>

There are several unique methods for the syntheses of  $\text{NiFe}_2\text{O}_4$  nanoparticles, including solid state reaction method,<sup>15</sup> reverse micelle method, sol-gel method,<sup>16</sup> hydrothermal techniques,<sup>17</sup> shock wave method,<sup>18</sup> aerosolization,<sup>19</sup> microwave hydrothermal method,<sup>20</sup> ultra-sonic hydrothermal method,<sup>21</sup> sonochemistry<sup>22</sup> and ball milling method.<sup>23</sup> The basic drawbacks of these techniques include the precision in maintaining the particle size and distribution. In the presence of atmospheric oxygen, oxidation of the particles is shielded to prevent agglomeration of  $\text{NiFe}_2\text{O}_4$  nanoparticles by coating them with special kinds of surfactants like sodium dodecyl sulphate and oleic acid.<sup>24</sup> The co-precipitation method has a peculiar advantage over all other methods for the synthesis of nanoparticles in that it does not require additional microwave heating and it is easy to control the size and size distribution.<sup>5</sup>

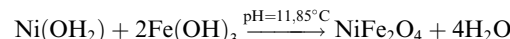
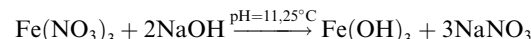
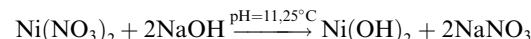
In this study, the co-precipitation technique was used to synthesize  $\text{NiFe}_2\text{O}_4$  nanoparticles. The particle size of the nanoparticles was tuned by using surfactants such as cetyltrimethyl ammonium bromide (CTAB) and sodium dodecyl benzene sulphonate (SDS). X-ray diffraction (XRD), Fourier transform infrared (FTIR), scanning electron microscopy (SEM), and atomic force microscopy (AFM). The electrochemical properties of the nanoparticles were studied by employing different electroanalytical techniques such as cyclic voltammetry (CV), galvanic charge-discharge (GCD) and electrochemical impedance spectroscopy (EIS), which confirmed that the  $\text{NiFe}_2\text{O}_4$ @CTAB, having smaller particle size coupled with larger surface area can be used as potential electrode material for futuristic energy storage devices.

## 2. Materials and methods

### 2.1. Chemical synthesis

**2.1.1. Synthesis of nickel ferrite ( $\text{NiFe}_2\text{O}_4$ ) nanoparticles.** Nickel ferrite NPs were synthesized using a modified wet chemical co-precipitation method.  $0.4 \text{ M}$  ferric nitrates and

$0.2 \text{ M}$  nickel nitrate solutions in equal volume ratio were mixed in a three-neck round bottom flask. The initial pH of the mixed binary solution was recorded as 1.34. To initiate the chemical reaction,  $3 \text{ M NaOH}$  (as precipitant) was added dropwise in the mixed solution with constant stirring to achieve a pH close to 11. The grayish-black residue of ferrite NPs appeared in the reaction mixture which was heated up to  $85^\circ\text{C}$  for 90 minutes. The solid nickel ferrite NPs were washed many times with distilled water and ethanol and dried in an oven at  $65^\circ\text{C}$  for 48 hours.



**2.1.2. Synthesis of nickel ferrite NPs with the assistance of surfactants.** To examine the effect of surfactants on the synthesis of nickel ferrite NPs, 8–10 drops of  $0.04 \text{ M}$  solution of surfactants, cetyltrimethylammonium bromide (CTAB), or sodium dodecylbenzene sulphonate (SDS) were added during co-precipitation. The temperature of the reaction mixture was increased to  $80^\circ\text{C}$  for 90 minutes. The resultant black residue was washed with distilled water and ethanol to remove excess ions (nitrate and sodium) and the product was dried in an oven at  $65^\circ\text{C}$  for two days. The surfactant-assisted prepared nickel ferrite products were labeled as NFNPs@CTAB (with cetyltrimethylammonium bromide) and NFNPs@SDS (with sodium dodecylbenzene sulphonate) for further characterization and electrochemical application.

### 2.2. Characterization

**2.2.1. Crystallographic study of nickel ferrite ( $\text{NiFe}_2\text{O}_4$ ).** X-ray diffraction (XRD) technique was used to identify the effects of cationic and anionic capping agents on the surface morphology of nickel ferrite nanoparticles (NFNPs). XRD patterns of pure and surfactant-assisted NFNPs are shown in Fig. 1A. All the diffraction peaks are in correspondence with diffraction angles at  $17.99^\circ$ ,  $30.10^\circ$ ,  $34.94^\circ$ ,  $37.01^\circ$ ,  $42.86^\circ$ ,  $54.05^\circ$ ,  $57.01^\circ$  and  $61.89^\circ$  and are parallel with JCPDS card no (22-1086) ratifying the cubic inverse spinel phase structure of native NFNPs. The space group symmetry  $Fd3m$ ,  $O_h$  and powder crystalline morphology of pure nickel ferrite NPs showed their high purity index.<sup>24,25</sup> Sharp XRD peaks at (111), (220), (311), (222), (400), (422), (511) and (440) are also justifying the crystalline index of NFNPs. The average size of pure nickel ferrite nano-crystals was  $46 \text{ nm}$  as measured from widely distributed diffraction peak (311) using Debye Sherrer eqn (1).

$$D = 0.9\lambda/\beta \cos \theta \quad (1)$$

where  $D$  is the crystal diameter,  $\lambda$  is the wavelength of  $\text{CuK}\alpha$  X-ray,  $\beta$  is FWHM diffracted rays and  $\theta$  is the Bragg's angle.<sup>26</sup>



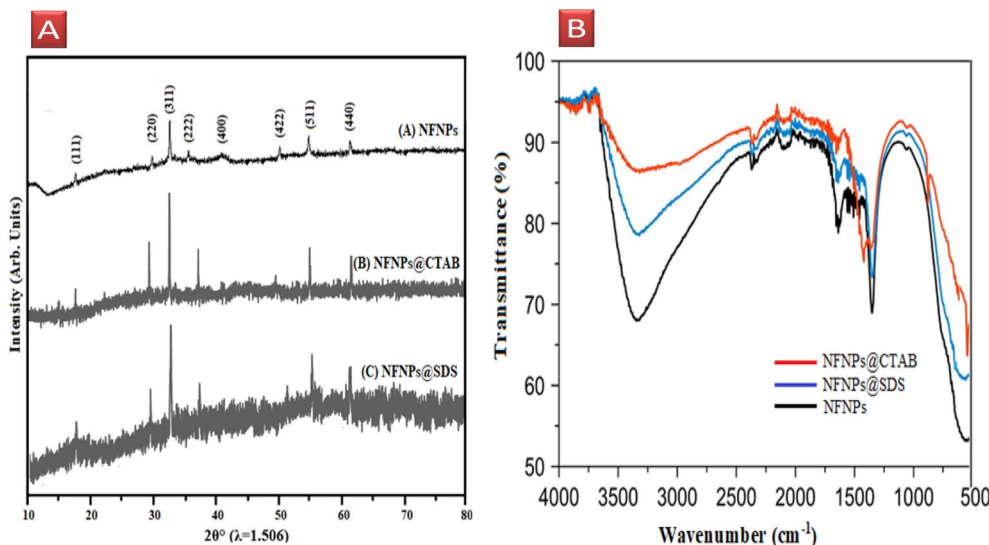


Fig. 1 (A) XRD patterns and (B) FT-IR spectrum of native  $\text{NiFe}_2\text{O}_4$  and surfactant-assisted  $\text{NiFe}_2\text{O}_4@\text{CTAB}$ ,  $\text{NiFe}_2\text{O}_4@\text{SDS}$  nanoparticles.

The addition of surfactants has a significant impact on the regular arrangement of the particles on crystal growth as well as the size of NFNPs. The presence of a long alkyl hydrocarbon chain in both surfactants acts as an impurity and induces an amorphous nature in regular lattice points of ferrite nanoparticles. The presence of surfactants serves as a capping agent, effectively minimizing the particle size of nickel ferrite nanoparticles (NFNPs) to approximately 22 nm and 27 nm with NFNPs@CTAB and NFNPs@SDS, respectively. This size reduction was determined using the Debye–Sherrer equation. In the case of CTAB and SDS, the broadening of the diffraction peak (311) indicates the impact of capping agents in preventing NP clustering, ultimately resulting in a reduction in the particle size. Huang *et al.* also observed diffraction peak broadening at (311) when ferrite particle size was decreased to below 20 nm.<sup>27</sup> Nickel ferrite NPs prepared using a cationic surfactant (NFNPs@CTAB) have a pronounced effect on size reduction as compared to those prepared using the anionic surfactant. The adsorbed hydroxide ions on the surface of ferrite particles promote the coating of cationic surfactants and enhance their dispersion by reducing agglomeration. So, cationic surfactants are more capable of dispersing and decreasing particle size of nickel ferrite NPs as compared to the anionic one.

**2.2.2. FTIR spectrum of pure and surfactant-assisted nickel ferrite NPs.** To identify the distinctive vibrations of metal ions within their lattice structures, a Fourier transform-infrared (FTIR) spectrum was examined within the range of 4000–500  $\text{cm}^{-1}$ . The FTIR spectra of both pure as well as surfactant-enhanced nickel ferrite nanoparticles (NPs) are depicted in Fig. 1B. The broad absorption band between 3200–3600  $\text{cm}^{-1}$  indicates the presence of moisture content in the samples and the vibrations of water molecules  $-\text{OH}$  groups absorbed on the ferrite NP surface. The presence of a characteristic metal–oxygen peak (600–500  $\text{cm}^{-1}$ ) is evident in all IR spectra, confirming the precise preparation of nickel ferrite in both the absence and presence of surfactants. A spectral peak at

508  $\text{cm}^{-1}$  signifies the native stretching vibrations of the metal–oxygen interaction in the metal ferrite at tetrahedral ( $T_h$ ) and octahedral ( $O_h$ ) positions.<sup>28</sup> The peaks at 850  $\text{cm}^{-1}$  and 1000–1400  $\text{cm}^{-1}$  for the surfactant-coated nickel ferrite NPs indicate the presence of  $-\text{CH}_2$  and C–O, C–H linkages, respectively, within the surfactant (CTAB and SDS) structures.<sup>29,30</sup>

**2.2.3. Microscopic studies of pure and surfactant-assisted nickel ferrite NPs.** To probe the effect of surfactants on the surface topography, morphology and size reduction of nickel ferrite nanoparticles, various microscopic studies including dynamic light scattering, atomic force microscopy, elemental mapping, scanning electron microscopy and transmission electron microscopy were performed and their images are shown in Fig. 2 and Fig. 3. Native nickel ferrite NPs having the size around  $\approx 45$  nm are spherical in shape and suffering from agglomeration effect as shown in AFM images. However, with the addition of CTAB and SDS, the stabilization of the ferrite particles enhanced with the decrease of nucleation growth as explained in the literature also.<sup>31</sup> The addition of the surfactants promotes the uniform distribution of the particles as shown in AFM, SEM and TEM images. Nickel ferrite NPs obtained using CTAB, are more uniformly distributed and reduced in their hydrodynamic size as compared to SDS. In fact, the nature of surfactants has a pronounced effect on reducing the particle size. The alkaline media of the reaction makes the particle negatively charged due to the adsorption of the hydroxyl groups ( $-\text{OH}$ ). Thus, the cationic capping agents such as CTAB are more effectively adsorbed at the surface of the particles to control their nucleation and growth, also called Ostwald's ripening. TEM studies of CTAB-coated nickel ferrite NPs (as shown in Fig. 3) were also performed to obtain a more precise idea about the role of CTAB on the surface morphology and controlled growth of nickel ferrite NPs. TEM images reveal spherical morphology of NFNPs as also confirmed by AFM and SEM. The average particle size (21 nm) as determined by TEM is very close to XRD calculations. The coagulation of ferrite NPs was also reduced by cationic CTAB

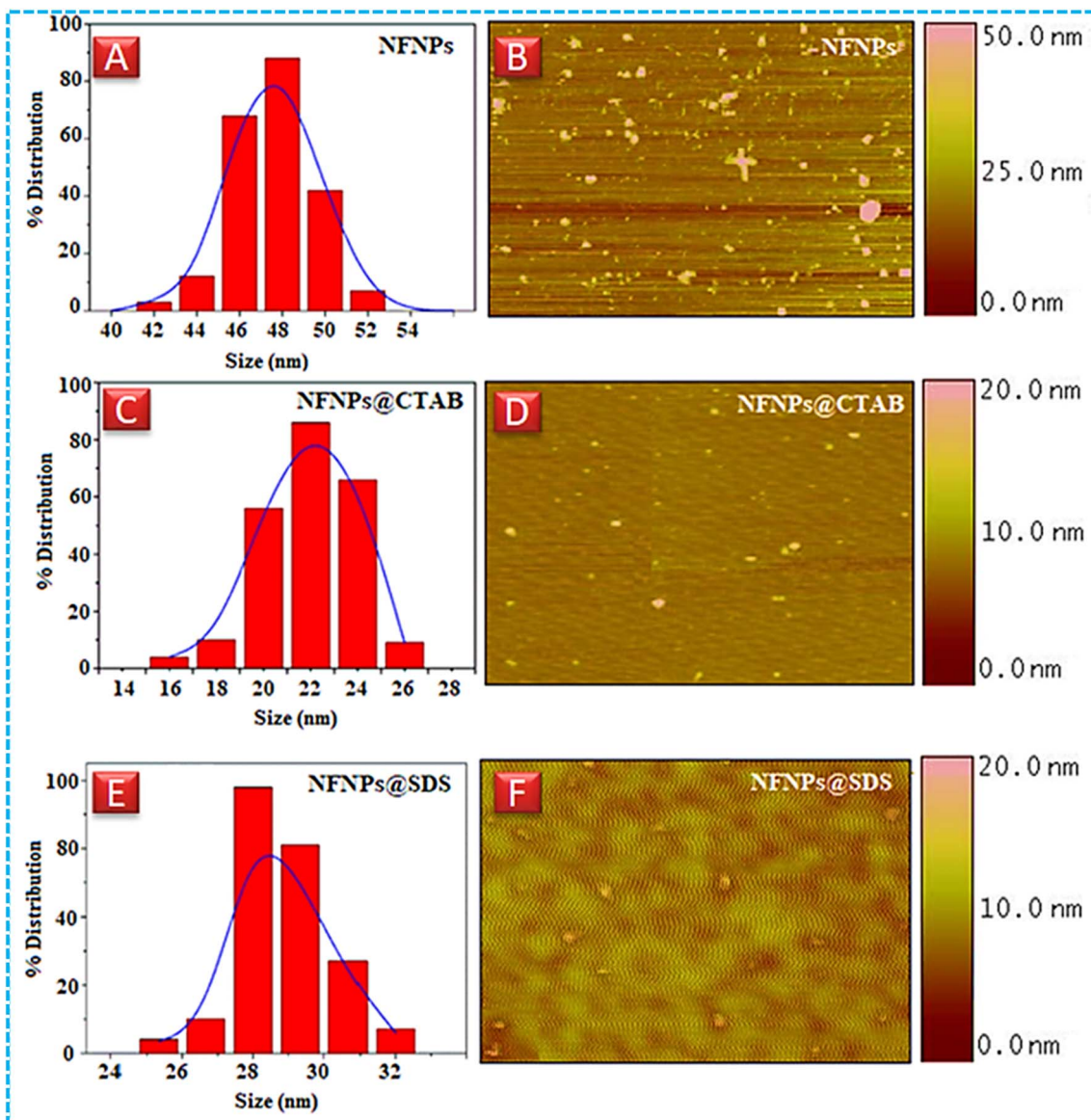


Fig. 2 Dynamic light scattering images of (A)  $\text{NiFe}_2\text{O}_4$  (C)  $\text{NiFe}_2\text{O}_4@\text{CTAB}$  (E)  $\text{NiFe}_2\text{O}_4@\text{SDS}$ , atomic force microscopy images (B)  $\text{NiFe}_2\text{O}_4$  (D)  $\text{NiFe}_2\text{O}_4@\text{CTAB}$ , and (F)  $\text{NiFe}_2\text{O}_4@\text{SDS}$ .

coating as shown in Fig. 3G-I. Elemental mapping images confirm the presence of Ni, Fe and oxygen in the nickel ferrite particles as shown in Fig. 3D-F. The nanoparticle size range of native and surfactant-assisted synthesized nickel ferrite NPs measured by various techniques is shown in Table 1.

### 2.3. Electrochemical analysis

Electrochemical analysis was performed on OrigaLys, France electrochemical work station OrigaFlex-OGF+01A, OGF+05A and OrigaFlex-OGFEIS using a three-electrode assembly with nickel ferrite NPs as the working electrode, platinum wire as counter electrode and silver-silver chloride ( $\text{Ag}/\text{AgCl}$ ) as the reference electrode. Electrochemical studies were conducted in 1 M KOH solution as an electrolyte. NFNPs working electrode was prepared by grinding the sample to a fine powder. Nickel

foam was used as a substrate material to deposit the nickel ferrite NPs. Prior to the deposition of the active material on NF, it was treated sequentially with 3 M HCl, acetone and ethanol. NFNPs, polyvinylidene fluoride (PVDF) binder and activated carbon (80 : 10 : 10) were mixed in *N*-methyl pyrrolidone (NMP) and stirred for 6 hours to prepare a homogeneous slurry. The drop casting method was employed to deposit the slurry onto the pre-treated NF and was kept for drying in an oven at 40 °C for 4 hours.

**2.3.1. Cyclic voltammetry.** Electrochemical measurements were taken by selecting the potential window ranging from 0 mV to 600 mV. Cyclic voltammetry was carried out at various scan rates (5, 10, 25, 50, 100, and 200 mV s<sup>-1</sup>) as shown in Fig. 4a. Oxidation and reduction peaks at negative and positive scans vividly depicted the existence of the redox mechanism. In nickel

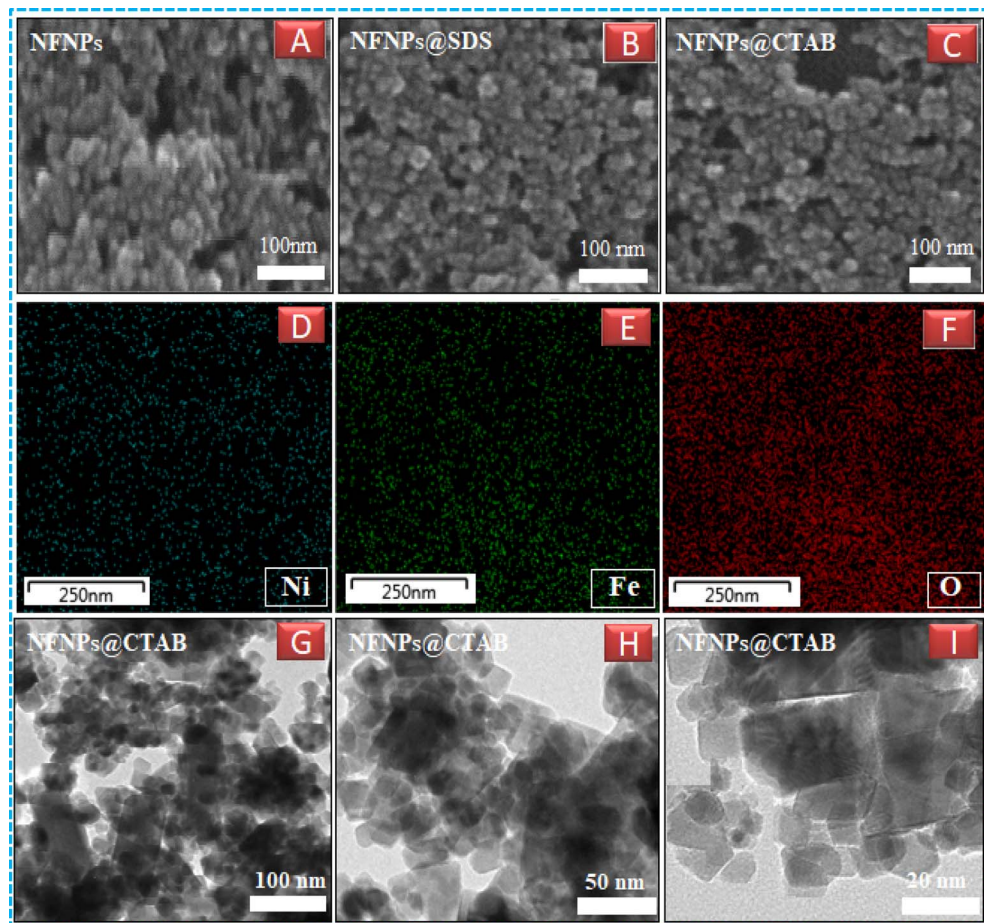


**Fig. 3** Scanning electron microscope images of (A)  $\text{NiFe}_2\text{O}_4$  (B)  $\text{NiFe}_2\text{O}_4@\text{SDS}$  (C)  $\text{NiFe}_2\text{O}_4@\text{CTAB}$ , Elemental mapping micrographs (D) nickel-K $\alpha$  (E) iron-K $\alpha$  (F) oxygen-K $\alpha$ , Transmission electron microscope images of  $\text{NiFe}_2\text{O}_4@\text{CTAB}$  at (G) 100 nm (H) 50 nm, and (I) 20 nm.

**Table 1** Range of the particle size measured by various characterization techniques

Sample	TEM	DLS (nm)	PDI XRD (nm)	AFM (nm)
$\text{NiFe}_2\text{O}_4$	—	48	0.28 45	50
$\text{NiFe}_2\text{O}_4@\text{CTAB}$	21	24	0.11 22	20
$\text{NiFe}_2\text{O}_4@\text{SDS}$	—	28	0.19 27	30

ferrites, the conductivity was enhanced due to the interconversion of electrons between  $\text{Fe}^{2+}/\text{Fe}^{3+}$  and  $\text{Ni}^{2+}/\text{Ni}^{+}$ . A mathematical approach was used to discuss the faradaic nature of  $\text{NiFe}_2\text{O}_4$  NPs and a graph was plotted between the peak currents and square root of the scan rate Fig. 4b. The graphs have a regression coefficient of approximately equal to 1 that elaborated the presence of reversible redox reaction in NFNPs. Furthermore, power law (eqn (2)) was employed to study the relationship between peak oxidation peak current and reduction peak current *versus* the scan rate.<sup>32</sup>

$$i_p = av^b \quad (2)$$

where 'a' and 'b' are the variables,  $i_p$  is the peak current and  $v$  is the value of the scan rate. The plotted graph gave a straight line

and the slope of the graph showed the *b*-value Fig. 4c. The *b*-value has significance in evaluating the capacitive and battery-like nature of the material. If the *b*-value is near 1, it signifies the capacitive nature of the electrode, while on the other hand, the value of *b* closer to 0.5 denotes the diffusive nature of electrode material.<sup>25</sup>

CV plot remained the same at all the scan rates but only differed in the peak current after increasing the scan rate, which displays that the native  $\text{NiFe}_2\text{O}_4$  NPs working electrodes have excellent rate capability. Retention of the CV peak shape also signifies the electrochemical reversibility of the  $\text{NiFe}_2\text{O}_4$  NPs working electrode signifying the fast diffusion of charges between the electrode and electrolyte. The stability of  $\text{NiFe}_2\text{O}_4$  NPs can also be estimated by the linear increase in redox peak by increasing scan rate and electrochemical active components in  $\text{NiFe}_2\text{O}_4$  NPs enhance the conductivity of the electrode.

**2.3.2. Galvanostatic charge-discharge.** To investigate the charge capacity of  $\text{NiFe}_2\text{O}_4$  nanoparticles, galvanostatic charge-discharge measurements were taken at discrete current densities (2, 3, 4, 5 and 6 A g<sup>-1</sup>). In correspondence with the cyclic voltammetric measurements, the plateaus in GCD curves also showed the pseudocapacitive nature of  $\text{NiFe}_2\text{O}_4$  NPs. In charging curves, the current increased abruptly due to the



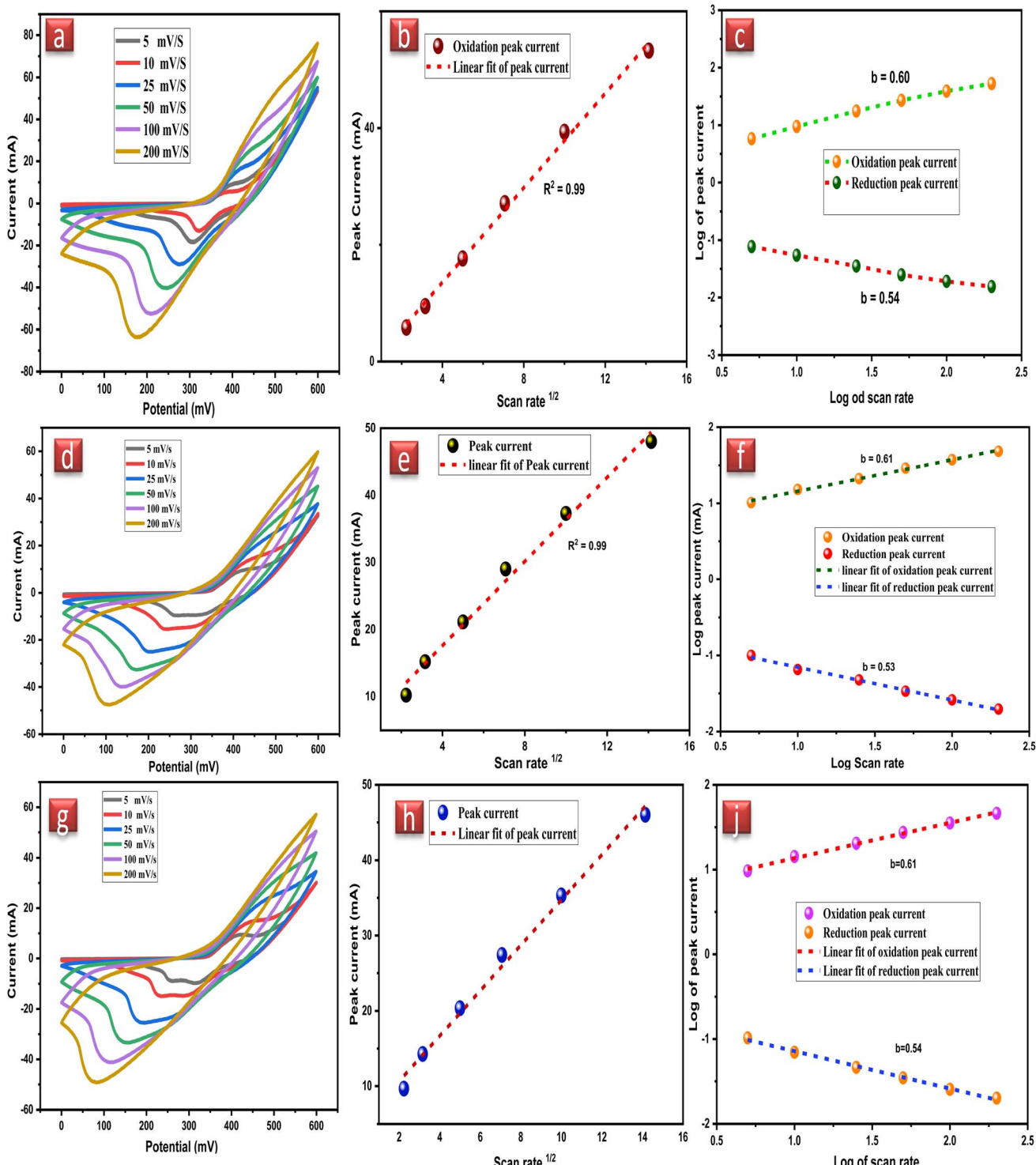


Fig. 4 (a) CV plot of native  $\text{NiFe}_2\text{O}_4$  NPs (b) linear regression coefficient of  $\text{NiFe}_2\text{O}_4$  NPs (c)  $b$  values of  $\text{NiFe}_2\text{O}_4$  NPs (d) CV plot of  $\text{NiFe}_2\text{O}_4@\text{CTAB}$  (e) linear regression coefficient of  $\text{NiFe}_2\text{O}_4@\text{CTAB}$  (f)  $b$ -values of  $\text{NiFe}_2\text{O}_4@\text{CTAB}$  (g) CV plot of  $\text{NiFe}_2\text{O}_4@\text{SDS}$  (h) linear regression coefficient of  $\text{NiFe}_2\text{O}_4@\text{SDS}$ , and (i)  $b$ -values of  $\text{NiFe}_2\text{O}_4@\text{SDS}$ .

capacitive nature that was followed by plateaus, which confirmed that the current contribution was changed as a result of the diffusive-controlled mechanism (Fig. 5A-C). The  $\text{NiFe}_2\text{O}_4$  NPs hold excellent reaction reversibility that could be confirmed

by the presence of symmetrical plateaus in the discharge curves. Specific capacities of native and surfactant-assisted NFNPs ( $\text{NiFe}_2\text{O}_4@\text{CTAB}$  and  $\text{NiFe}_2\text{O}_4@\text{SDS}$ ) were determined at different current densities using eqn (3), showing maximum

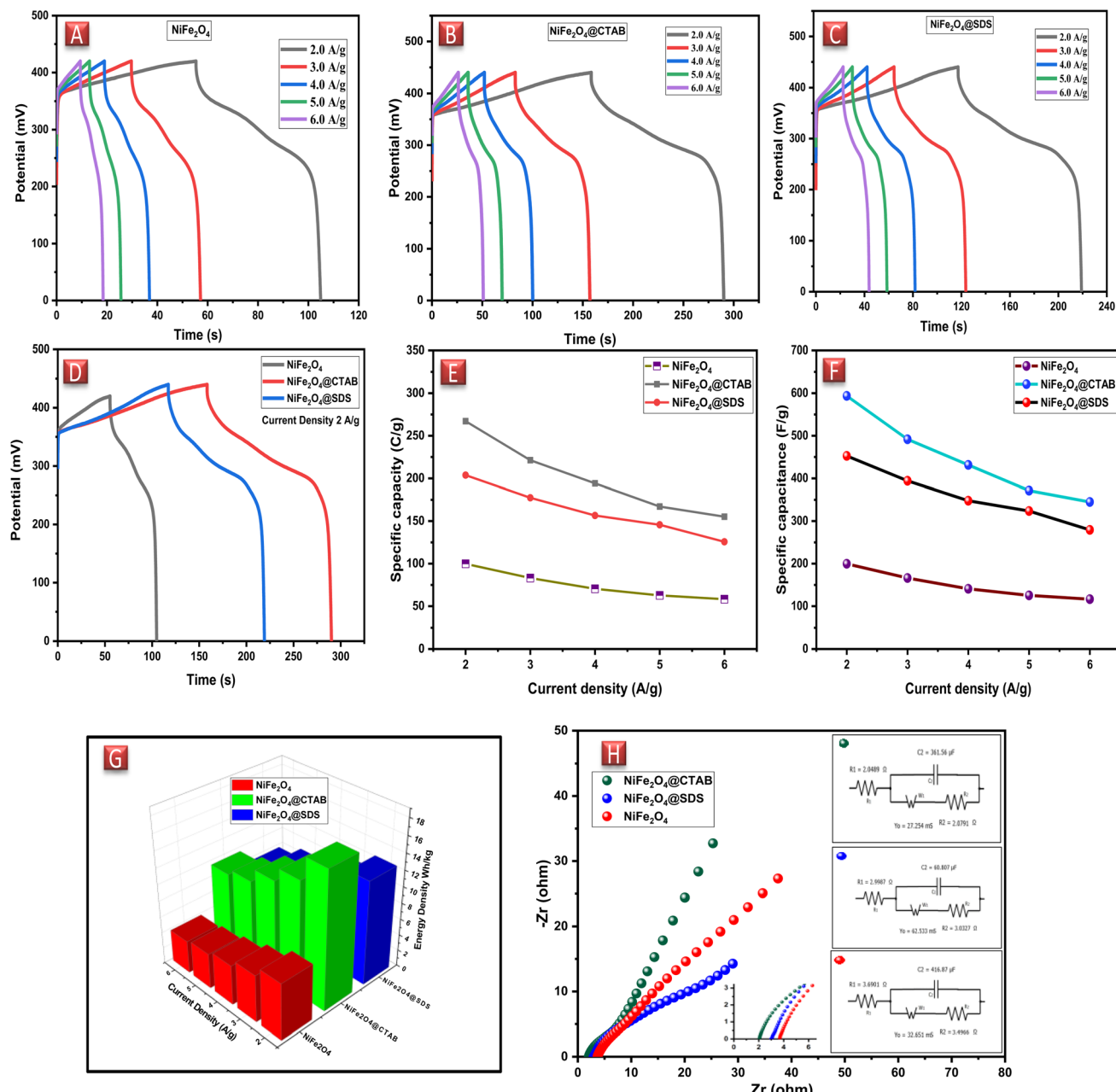


Fig. 5 (A) GCD measurements of NiFe<sub>2</sub>O<sub>4</sub>, (B) NiFe<sub>2</sub>O<sub>4</sub>@CTAB and (C) NiFe<sub>2</sub>O<sub>4</sub>@SDS. (D) Comparison of GCD curves, (E) specific capacities, (F) specific capacitance (G) bar-chart showing energy densities and (H) EIS plots of NiFe<sub>2</sub>O<sub>4</sub>, NiFe<sub>2</sub>O<sub>4</sub>@CTAB and NiFe<sub>2</sub>O<sub>4</sub>@SDS.

specific capacities of 99.8, 267.1 and 203.7 C g<sup>-1</sup>, respectively, at a current density of 2 A g<sup>-1</sup>, which decreased with increasing current density (Fig. 5E).<sup>33</sup>

The specific capacitances of the NFNPs were also determined using eqn (4), which were 199.6, 593.6 and 452.3 F g<sup>-1</sup> for native NiFe<sub>2</sub>O<sub>4</sub>, NiFe<sub>2</sub>O<sub>4</sub>@CTAB and NiFe<sub>2</sub>O<sub>4</sub>@SDS, respectively, at a current density of 2 A g<sup>-1</sup>, which decreased with increasing current density (Fig. 5F).<sup>26</sup>

$$Q_s = \frac{I \times E_t}{m} \quad (3)$$

$$C_s = \frac{I \times \Delta t}{m \times V} \quad (4)$$

Here, the expression  $I/m$  indicates the current density and  $\Delta t$  signifies the discharge time of the GCD curve. From the specific capacity values determined from GCD analysis, energy density and power density were calculated by using eqn (5) and (6).<sup>34</sup>

$$E_s = \frac{Q_s \times \Delta v}{2 \times 3.6} \quad (5)$$

$$P_s = \frac{E \times 3600}{\Delta t} \quad (6)$$

Table 2 Comparison of specific capacities, specific capacitances, energy densities and power densities of NFNPs

Sample	Specific capacity (C g <sup>-1</sup> ) at 2 A g <sup>-1</sup>	Specific capacitance (F g <sup>-1</sup> ) at 2 A g <sup>-1</sup>	Energy density (W h kg <sup>-1</sup> ) 2 A g <sup>-1</sup>	Power density (W h kg <sup>-1</sup> ) at 6 A g <sup>-1</sup>
NiFe <sub>2</sub> O <sub>4</sub>	99.8	199.6	6.93	1200
NiFe <sub>2</sub> O <sub>4</sub> @CTAB	267.1	593.6	16.69	1420
NiFe <sub>2</sub> O <sub>4</sub> @SDS	203.7	452.3	12.73	1350

Native NFNPs, NiFe<sub>2</sub>O<sub>4</sub>@CTAB and NiFe<sub>2</sub>O<sub>4</sub>@SDS showed the maximum energy density of 6.93, 16.69 and 12.73 W h kg<sup>-1</sup> and power densities of 1200, 1420 and 1350 W kg<sup>-1</sup>, respectively, at a current density of 2 A g<sup>-1</sup>. A comparison of electrochemical parameters of the synthesized native NiFe<sub>2</sub>O<sub>4</sub>, NiFe<sub>2</sub>O<sub>4</sub>@CTAB and NiFe<sub>2</sub>O<sub>4</sub>@SDS is shown in Table 2.

**2.3.3. Electrochemical impedance spectroscopy.** To evaluate the inclusive conductivity of NiFe<sub>2</sub>O<sub>4</sub> NPs electrode electrochemical impedance spectroscopy was employed. EIS was carried out in an AC frequency range of 0.1 Hz to 100 KHz and Nyquist plots of three samples were taken (Fig. 5H). The EIS spectrum showed that there was small equivalent solution resistance ( $E_{SR}$ ) due to ions diffusion through the electrolyte and the interface resistance of the electrode. Moreover, in the domain of higher frequencies, the presence of semicircle indicated the charge transfer resistance ( $R_{ct}$ ), which can be obtained from equivalent circuits.<sup>14,27</sup> Charge transfer resistance also known as Faraday's resistance is faced by electrochemical reactions on the interface of the NiFe<sub>2</sub>O<sub>4</sub> NPs electrode.

In the case of the NiFe<sub>2</sub>O<sub>4</sub> NP electrode, the values of  $E_{SR}$  and  $R_{ct}$  were recorded as 3.69 Ω and 3.49 Ω, respectively. The straight line signified the Warburg impedance indicating ion diffusion and pseudocapacitive behavior of the electrode material (in red). NiFe<sub>2</sub>O<sub>4</sub>@SDS exhibited an  $E_{SR}$  of 2.99 Ω with an  $R_{ct}$  of 3.03 Ω (in blue). While NiFe<sub>2</sub>O<sub>4</sub>@CTAB indicated an  $E_{SR}$  value of 2.05 Ω with a small semicircle showing the negligible  $R_{ct}$  of 2.08 Ω, which advocated the positive effect of CTAB on the NiFe<sub>2</sub>O<sub>4</sub> NPs (in green). The presence of Warburg resistance also proved the pseudocapacitive nature of the electrode material.

### 3. Conclusions

Herein, we have reported the synthesis of nickel ferrite nanoparticles by controlling surface area utilizing different surfactants; cationic surfactant (CTAB) and anionic surfactant (SDS). Different structural analysis techniques confirmed that CTAB proved a more promising tool to control surface topography, morphology, particle size and dispersion of nickel ferrite NPs. Electrochemical techniques such as CV, GCD and EIS were used to evaluate the electrochemical performance of the synthesized materials. Native NFNPs, NiFe<sub>2</sub>O<sub>4</sub>@CTAB and NiFe<sub>2</sub>O<sub>4</sub>@SDS showed specific capacity as 99.8, 267.1, 203.7 C g<sup>-1</sup>, specific capacitance as 199.6, 593.6, 452.3 F g<sup>-1</sup>, energy density of 6.93, 16.69, 12.73 W h kg<sup>-1</sup> and power density of 1200, 1420 and 1350 W kg<sup>-1</sup>, respectively. The results illustrated that the reduced particle size coupled with a larger surface area of NFNPs@CTAB enhanced the electrochemical performance of nickel ferrite nanoparticles as a potential candidate for

electrode material in the field of electrochemical energy storage devices.

### Author contributions

Muhammad Waheed wrote the manuscript. Shahbaz performed the electrochemical analysis. Rabia performed the experiments. Shahid critically proofed the manuscript. Shahzad designed the study, Kainat performed the synthesis and Naveed prepared the graphs.

### Conflicts of interest

The authors declare that they have no known competing financial interests or personal relationships that could have appeared to influence the work reported in this paper.

### Acknowledgements

We acknowledge financial assistance from the Higher Education Commission (HEC) of Pakistan, HEC-NRPU project no. 20-17612/NRPU/R&D/HEC/2021. We are grateful to Dr Mustansar Abbas for the X-ray studies.

### References

- 1 D. H. Chen and X. R. He, Synthesis of nickel ferrite nanoparticles by sol-gel method, *Mater. Res. Bull.*, 2001, **36**(7-8), 1369-1377, DOI: [10.1016/S0025-5408\(01\)00620-1](https://doi.org/10.1016/S0025-5408(01)00620-1).
- 2 Z. Karcioğlu Karakaş, R. Boncukcuoğlu, İ. H. Karakaş and M. Ertuğrul, The effects of heat treatment on the synthesis of nickel ferrite (NiFe<sub>2</sub>O<sub>4</sub>) nanoparticles using the microwave assisted combustion method, *J. Magn. Magn. Mater.*, 2015, **374**, 298-306, DOI: [10.1016/j.jmmm.2014.08.045](https://doi.org/10.1016/j.jmmm.2014.08.045).
- 3 V. Šepelák, D. Baabe, D. Mienert, *et al.*, Evolution of structure and magnetic properties with annealing temperature in nanoscale high-energy-milled nickel ferrite, *J. Magn. Magn. Mater.*, 2003, **257**(2-3), 377-386, DOI: [10.1016/S0304-8853\(02\)01279-9](https://doi.org/10.1016/S0304-8853(02)01279-9).
- 4 C. Ramankutty and S. Sugunan, Surface properties and catalytic activity of ferrospinels of nickel, cobalt and copper, prepared by soft chemical methods, *Appl. Catal., A*, 2001, **218**(1-2), 39-51, DOI: [10.1016/S0926-860X\(01\)00610-X](https://doi.org/10.1016/S0926-860X(01)00610-X).
- 5 K. Maaz, S. Karim, A. Mumtaz, S. K. Hasanain, J. Liu and J. L. Duan, Synthesis and magnetic characterization of nickel ferrite nanoparticles prepared by co-precipitation



route, *J. Magn. Magn. Mater.*, 2009, **321**(12), 1838–1842, DOI: [10.1016/j.jmmm.2008.11.098](https://doi.org/10.1016/j.jmmm.2008.11.098).

6 T. N. Pham, T. Q. Huy and A. T. Le, Spinel ferrite ( $\text{AFe}_2\text{O}_4$ )-based heterostructured designs for lithium-ion battery, environmental monitoring, and biomedical applications, *RSC Adv.*, 2020, **10**(52), 31622–31661, DOI: [10.1039/DORA05133K](https://doi.org/10.1039/DORA05133K).

7 R. Kumar, R. Kumar, P. Kumar Sahoo, M. Singh and A. Soam, Synthesis of nickel ferrite for supercapacitor application, *Mater. Today: Proc.*, 2022, **67**, 1001–1004, DOI: [10.1016/j.matpr.2022.05.433](https://doi.org/10.1016/j.matpr.2022.05.433).

8 N. Kumar, A. Kumar, G. M. Huang, W. W. Wu and T. Y. Tseng, Facile synthesis of mesoporous  $\text{NiFe}_2\text{O}_4$ /CNTs nanocomposite cathode material for high performance asymmetric pseudocapacitors, *Appl. Surf. Sci.*, 2018, **433**, 1100–1112, DOI: [10.1016/j.apsusc.2017.10.095](https://doi.org/10.1016/j.apsusc.2017.10.095).

9 A. Soam, R. Kumar, P. K. Sahoo, *et al.*, Synthesis of Nickel Ferrite Nanoparticles Supported on Graphene Nanosheets as Composite Electrodes for High Performance Supercapacitor, *ChemistrySelect*, 2019, **4**(34), 9952–9958, DOI: [10.1002/slct.201901117](https://doi.org/10.1002/slct.201901117).

10 X. Gao, W. Wang, J. Bi, *et al.*, Morphology-controllable preparation of  $\text{NiFe}_2\text{O}_4$  as high performance electrode material for supercapacitor, *Electrochim. Acta*, 2019, **296**, 181–189, DOI: [10.1016/j.electacta.2018.11.054](https://doi.org/10.1016/j.electacta.2018.11.054).

11 T. Arun, T. Kavinkumar, R. Udayabhaskar, *et al.*,  $\text{NiFe}_2\text{O}_4$  nanospheres with size-tunable magnetic and electrochemical properties for superior supercapacitor electrode performance, *Electrochim. Acta*, 2021, **399**, 139346, DOI: [10.1016/j.electacta.2021.139346](https://doi.org/10.1016/j.electacta.2021.139346).

12 A. M. M. Farea, S. Kumar, K. M. Batoo, A. Yousef, C. G. Lee and K. Alimuddin, Influence of the doping of  $\text{Ti}^{4+}$  ions on electrical and magnetic properties of  $\text{Mn}_{1+x}\text{Fe}_{2-2x}\text{Ti}\text{O}_4$  ferrite, *J. Alloys Compd.*, 2009, **469**(1–2), 451–457, DOI: [10.1016/j.jallcom.2008.01.139](https://doi.org/10.1016/j.jallcom.2008.01.139).

13 S. Kumar, F. Ahmed, N. M. Shaalan, *et al.*, Structural, Magnetic, and Electrical Properties of  $\text{CoFe}_2\text{O}_4$  Nanostructures Synthesized Using Microwave-Assisted Hydrothermal Method, *Mater.*, 2022, **15**(22), 7955, DOI: [10.3390/ma15227955](https://doi.org/10.3390/ma15227955).

14 C. Hu, X. Yang, P. Liu, *et al.*, Multi-electron bipolar-type organic molecules for high-capacity dual-ion zinc batteries, *J. Mater. Chem. A*, 2024, **12**, 11867–11874, DOI: [10.1039/D4TA00476K](https://doi.org/10.1039/D4TA00476K).

15 A. Kale, S. Gubbala and R. D. K. Misra, Magnetic behavior of nanocrystalline nickel ferrite synthesized by the reverse micelle technique, *J. Magn. Magn. Mater.*, 2004, **277**(3), 350–358, DOI: [10.1016/j.jmmm.2003.11.015](https://doi.org/10.1016/j.jmmm.2003.11.015).

16 M. George, J. A. Mary, S. S. Nair, P. A. Joy and M. R. Anantharaman, Finite size effects on the structural and magnetic properties of sol-gel synthesized  $\text{NiFe}_2\text{O}_4$  powders, *J. Magn. Magn. Mater.*, 2006, **302**(1), 190–195, DOI: [10.1016/j.jmmm.2005.08.029](https://doi.org/10.1016/j.jmmm.2005.08.029).

17 D. Chen, D. Chen, X. Jiao, Y. Zhao and M. He, Hydrothermal synthesis and characterization of octahedral nickel ferrite particles, *Powder Technol.*, 2003, **133**(1–3), 247–250, DOI: [10.1016/S0032-5910\(03\)00079-2](https://doi.org/10.1016/S0032-5910(03)00079-2).

18 J. Liu, H. He, X. Jin, Z. Hao and Z. Hu, Synthesis of nanosized nickel ferrites by shock waves and their magnetic properties, *Mater. Res. Bull.*, 2001, **36**(13–14), 2357–2363, DOI: [10.1016/S0025-5408\(01\)00722-X](https://doi.org/10.1016/S0025-5408(01)00722-X).

19 M. A. Elmasry, A. Gaber and E. M. Khater, Preparation of nickel ferrite using the aerosolization technique, *Powder Technol.*, 1997, **90**(2), 161–164, DOI: [10.1016/S0032-5910\(96\)03216-0](https://doi.org/10.1016/S0032-5910(96)03216-0).

20 V. K. Sankaranarayanan and C. Sreekumar, Precursor synthesis and microwave processing of nickel ferrite nanoparticles, *Curr. Appl. Phys.*, 2003, **3**(2–3), 205–208, DOI: [10.1016/S1567-1739\(02\)00202-X](https://doi.org/10.1016/S1567-1739(02)00202-X).

21 P. E. Meskin, V. K. Ivanov, A. E. Barantchikov, B. R. Churagulov and Y. D. Tretyakov, Ultrasonically assisted hydrothermal synthesis of nanocrystalline  $\text{ZrO}_2$ ,  $\text{TiO}_2$ ,  $\text{NiFe}_2\text{O}_4$  and  $\text{Ni}_{0.5}\text{Zn}_{0.5}\text{Fe}_2\text{O}_4$  powders, *Ultrason. Sonochem.*, 2006, **13**(1), 47–53, DOI: [10.1016/j.ulsonch.2004.12.002](https://doi.org/10.1016/j.ulsonch.2004.12.002).

22 K. V. P. M. Shafi, Y. Koltypin, A. Gedanken, *et al.*, Sonochemical Preparation of Nanosized Amorphous  $\text{NiFe}_2\text{O}_4$  Particles, *J. Phys. Chem. B*, 1997, **101**(33), 6409–6414, DOI: [10.1021/jp970893q](https://doi.org/10.1021/jp970893q).

23 A. Azizi and S. K. Sadrnezhaad, Effects of annealing on phase evolution, microstructure and magnetic properties of mechanically synthesized nickel-ferrite, *Ceram. Int.*, 2010, **36**(7), 2241–2245, DOI: [10.1016/j.ceramint.2010.06.004](https://doi.org/10.1016/j.ceramint.2010.06.004).

24 T. Fried, G. Shemer and G. Markovich, Ordered Two-Dimensional Arrays of Ferrite Nanoparticles, *Adv. Mater.*, 2001, **13**(15), 1158–1161, DOI: [10.1002/1521-4095\(200108\)13:15<1158::AID-ADMA1158>3.0.CO;2-6](https://doi.org/10.1002/1521-4095(200108)13:15<1158::AID-ADMA1158>3.0.CO;2-6).

25 M. Shahbaz, S. Sharif, A. Shahzad, Z. S. Şahin, B. Riaz and S. Shahzad, Enhanced electrochemical performance of cerium-based metal organic frameworks derived from pyridine-2,4,6-tricarboxylic acid for energy storage devices, *J. Energy Storage*, 2024, **88**, 111463, DOI: [10.1016/j.est.2024.111463](https://doi.org/10.1016/j.est.2024.111463).

26 S. Sharif, J. H. Shah, M. Shahbaz, *et al.*, Structural, DFT and redox activity investigation of 2D silver based MOF for energy storage devices, *J. Electroanal. Chem.*, 2024, **961**, 118226, DOI: [10.1016/j.jelechem.2024.118226](https://doi.org/10.1016/j.jelechem.2024.118226).

27 Y. Zhang, Z. Song, L. Miao, Y. Lv, L. Gan and M. Liu, Non-Metallic  $\text{NH}_4^+/\text{H}^+$  Co-Storage in Organic Superstructures for Ultra-Fast and Long-Life Zinc-Organic Batteries, *Angew. Chem. Int. Ed.*, 2024, **63**(3), e202316835, DOI: [10.1002/anie.202316835](https://doi.org/10.1002/anie.202316835).

28 G. Wang, Y. Ma, J. Mu, *et al.*, Monodisperse polyvinylpyrrolidone-coated  $\text{CoFe}_2\text{O}_4$  nanoparticles: synthesis, characterization and cytotoxicity study, *Appl. Surf. Sci.*, 2016, **365**, 114–119, DOI: [10.1016/j.apsusc.2016.01.031](https://doi.org/10.1016/j.apsusc.2016.01.031).

29 M. Salavati-Niasari, F. Davar and T. Mahmoudi, A simple route to synthesize nanocrystalline nickel ferrite ( $\text{NiFe}_2\text{O}_4$ ) in the presence of octanoic acid as a surfactant, *Polyhedron*, 2009, **28**(8), 1455–1458, DOI: [10.1016/j.poly.2009.03.020](https://doi.org/10.1016/j.poly.2009.03.020).

30 K. Nejati and R. Zabihi, Preparation and magnetic properties of nano size nickel ferrite particles using hydrothermal



method, *Chem. Cent. J.*, 2012, **6**(1), 23, DOI: [10.1186/1752-153X-6-23](https://doi.org/10.1186/1752-153X-6-23).

31 M. Mushtaq, F. Kanwal, A. Batool, T. Jamil, M. Zia-ul-Haq, B. Ijaz, Q. Huang and Z. Ullah, Polymer-coated  $\text{CoFe}_2\text{O}_4$  nanoassemblies as biocompatible magnetic nanocarriers for anticancer drug delivery, *J. Mater. Sci.*, 2017, **52**, 9282–9293, DOI: [10.1007/s10853-017-1141-3](https://doi.org/10.1007/s10853-017-1141-3).

32 M. Sathiya, A. S. Prakash, K. Ramesha, J. Tarascon and A. K. Shukla,  $\text{V}_2\text{O}_5$ -Anchored Carbon Nanotubes for Enhanced Electrochemical Energy Storage, *J. Am. Chem. Soc.*, 2011, **133**(40), 16291–16299, DOI: [10.1021/ja207285b](https://doi.org/10.1021/ja207285b).

33 M. Zahir Iqbal, M. Waqas Khan, M. Shaheen, *et al.*, 1,2,4,5-Benzene-tetra-carboxylic acid and 2-methylimidazole bi-linker intercalated redox active copper organic framework for advanced battery-supercapacitor hybrids, *J. Electroanal. Chem.*, 2023, **941**, 117505, DOI: [10.1016/j.jelechem.2023.117505](https://doi.org/10.1016/j.jelechem.2023.117505).

34 M. Z. Iqbal, M. W. Khan, M. Shaheen, *et al.*, Cobalt intercalated redox active 1,2,4,5-benzene-tetra-carboxylic acid-pyridine-3,5-dicarboxylic acid bi-linker organic framework for state-of-the-art battery-supercapacitor hybrids, *Mat. Today Sustainability*, 2023, **21**, 100286, DOI: [10.1016/j.mtsust.2022.100286](https://doi.org/10.1016/j.mtsust.2022.100286).

